TOMSK POLYTECHNIC UNIVERSITY

Available online at www.sciencedirect.com

ScienceDirect

Resource-Efficient Technologies 2 (2016) S12–S24

www.elsevier.com/locate/reffit

Research paper

Dry sliding wear studies of aluminum matrix hybrid composites

V.V. Monikandan *, M.A. Joseph, P.K. Rajendrakumar

Department of Mechanical Engineering, National Institute of Technology, Calicut 673601, Kerala, India

Received 6 June 2016; received in revised form 1 October 2016; accepted 5 October 2016

Available online 9 November 2016

Abstract

In the present work, hybrid composites are fabricated with self-lubricating characteristics to make them as resource-efficient materials. AA6061-10 wt. % B_4C–MoS_2 hybrid composites reinforced with 2.5, 5 and 7.5 wt. % concentration of MoS_2 particles are produced using stir casting technique, and mechanical and tribological properties are evaluated. Microstructural characterization of the hybrid composites revealed the uniform distribution of reinforcement (B_4C and MoS_2) particles in the matrix material. Hardness and fracture toughness of the hybrid composites are decreased monotonously with an increase in the addition of MoS_2 particles. Dry sliding tribological studies conducted using a pin-on-disk tribotester under atmospheric conditions revealed the formation of MoS_2-lubricated tribolayer on the worn pin surface which significantly influenced the tribological properties. The addition of MoS_2 particles decreased the friction coefficient and wear rate of the hybrid composites. Delamination and abrasion are observed to be the controlling wear mechanisms and material in the form of platelet-shaped debris, and flow-type chip debris is formed, and a long and shallow crater on the worn pin surface of the hybrid composite is also observed.

Keywords: AA6061-B_4C–MoS_2 composites; Solid lubrication; Stir casting; Tribological studies

1. Introduction

Aluminum alloys are broadly used in the automotive sector because of their high strength to weight ratio, suitability to cast into leak proof parts, ability to resist mechanical forces at temperatures near 145 °C and high thermal conductivity [1]. Monolithic aluminum alloys exhibit poor wear behavior compared to the particle reinforced Aluminum Matrix Composites (AMCs) [2,3]. The literature on B_4C reinforced Metal Matrix Composites (MMCs) is sparse because of the higher cost of B_4C particles compared to the conventional ceramic particles such as SiC particles [4] and Al_2O_3 particles [5]. Kennedy [4] observed that large specific property improvements of MMCs could be attained by using B_4C particles as the reinforcement phase. Hence, an AA6061-10 wt. % B_4C mono composite was produced using liquid metallurgy stir casting technique, and its tribological properties were studied [6]. Solid lubrication property was imparted by reinforcing the mono MMC with solid lubricants such as molybdenum disulfide (MoS_2), graphite (Gr) and tungsten disulfide (WS_2). In dry environmental conditions, the use of MoS_2 particles as a solid lubricant was shown to be far more suitable than Gr particles [7]. During stir casting, the addition of 4% Mg to improve the wettability of MoS_2 and SiC particles with the aluminum matrix material resulted in considerable improvement in ultimate tensile strength and hardness of the Al–SiC–MoS_2 hybrid composites [8].

Literature was reviewed to observe the influence of MoS_2 particles on the mechanical properties of MoS_2 reinforced composites. Deng et al. [9] observed that the hardness, flexural strength and fracture toughness of Al_2O_3–TiO_2–MoS_2 hybrid composites are decreased with increase in MoS_2 addition due to the formation of pores generated by the melting and escaping of MoS_2 particles during the hot pressing process. The sintering temperature employed for hot pressing of the hybrid composite specimen was 1700 °C. Kato et al. [10] studied the hardness and bending strength of Cu–Sn–MoS_2 composites and observed that both the hardness and bending strength were increased while the concentration of MoS_2 particles was up to 5 vol. %. However, as the concentration was increased beyond 5 vol. %, both the hardness and bending strength were decreased.

Several studies were conducted to assess the role of MoS_2 particles in the tribological properties of MoS_2 reinforced composites. Dharmalingam et al. [11] statistically analyzed the

* Corresponding author. Department of Mechanical Engineering, National Institute of Technology, Calicut 673601, Kerala, India. Fax: +91 495 228 7250.

E-mail addresses: saai.manikandan@gmail.com, p110059me@nitc.ac.in (V.V. Monikandan).

http://dx.doi.org/10.1016/j.reffit.2016.10.002

tribological properties of Al–Al_2O_3–MoS_2 composites that were slid against EN 32 counterface and observed that the specific wear rate and friction coefficient were significantly influenced by the addition of MoS_2 particles. Also, Dharmalingam et al. [12] studied the abrasive wear behavior of Al–Al_2O_3–MoS_2 composites and reported that both the wear rate and friction coefficient were decreased with increased content of MoS_2 particles. In both the studies, the Al–Al_2O_3–MoS_2 composites were fabricated through stir casting technique. Dry sliding tribological tests of Ag–Cu–MoS_2 composites mated against Ag–Cu counter disc revealed the formation of MoS_2-rich transfer layer which reduced the wear loss and friction coefficient of the composites. Delamination and abrasion were stated to be the dominant wear mechanisms that influenced the tribological behavior of the Ag–Cu–MoS_2 composites within the applied load range of 1–4 N [13]. A study of the tribological properties of Cu–MoS_2 and Cu–$MoSe_2$ composites that were mated against Cu counterface revealed the incurrence of adhesive wear. It was also observed that the solid lubrication becomes more significant for the composites having MoS_2 or $MoSe_2$ concentration greater than 5 wt. % [14]. Dhanasekaran and Gnanamoorthy [15] studied the tribological properties of Fe–Cu–C alloy containing MoS_2 particles, and it was observed that the composites exhibit better tribological properties up to 3 vol. % of MoS_2 particles addition. However, the composites exhibit poor tribological properties as the concentration of MoS_2 particles is increased to 5 vol. %.

Literature mentioned above makes it clear that the environment of testing, concentration of MoS_2 particles and the formation of MoS_2-lubricated tribolayer influence the tribological properties of the materials added with MoS_2 particles. It is understood that the mechanical properties are also influenced by the concentration of MoS_2 particles. In this work, particle-reinforced AA6061-B_4C–MoS_2 hybrid composites with various MoS_2 concentrations are fabricated, and their tribological and mechanical properties are studied. Also, the mechanical and tribological properties of the hybrid composites are compared with those of the AA6061-10 wt. % B_4C mono composite [6] to understand the influence of MoS_2 particles addition. Due to their self-lubricating properties, Al–B_4C–MoS_2 hybrid composites can be possible materials to fabricate different automotive components and also their self-lubricating characteristics can eliminate the need for external lubrication system during sliding.

2. Fabrication of hybrid composites

The casting method used to fabricate the hybrid composites, as well as the materials used for the fabrication, is detailed in the following sections.

2.1. Materials

AA6061 (Mg – 0.86, Si – 0.67, Fe – 0.19, Cu – 0.21, Ti – 0.018, Mn – 0.04, Cr – 0.05, Zn – 0.004, B – 0.003, Pb – 0.001, and the rest Al by wt. %), supplied by M/s. Hindalco Ind. Ltd., India, is selected as the primary phase. B_4C particles (supplied by M/s. Bhukhanvala Ind. Pvt. Ltd., India) of 30 μm Average Particle Size (APS) and MoS_2 particles (supplied by M/s. Otto Chemie Pvt. Ltd., India) of 130 μm APS are selected as the secondary phase.

2.2. Stir casting

Fig. 1(a) shows the macrograph of the stir casting equipment that is used to fabricate AA6061-10 wt. % B_4C–MoS_2 hybrid composites reinforced with 2.5, 5, and 7.5 wt. % MoS_2 particles through stir casting. The crucible and stirrer are made of stainless steel, and the permanent mold and skimmer are made of mild steel. The stir casting process is carried out in a step by step procedure. The crucible, stirrer, permanent mold, and skimmer are coated with coatings that have water as carrier and vermiculite and refractory pigments as concentrates. The coating prevents the reaction between the melt and the metallic components that come into contact with the melt. The coated components are heated to 180 °C to evaporate the carrier (water) after coating. Time (10 min) is given for the evaporation to complete, and then the argon gas is supplied continuously to the crucible to prevent the reaction of matrix material with the atmospheric air. AA6061 alloy bars cleaned with acetone are placed inside the crucible, and the electric furnace is heated to 800 °C that is higher than the melting point (621 °C) of the AA6061 alloy to compensate for the heat loss incurred due to stirring [6]. The temperature at which the addition of the reinforcement particles, stirring, and pouring are carried out, is above the liquidus temperature of the melt [6]. The melt temperature is maintained at a precision of ±2 °C throughout the casting process. 1 wt. % of magnesium (Mg) is added to the melt in the form of Al–Mg master alloy to enhance the wettability of the reinforcement particles with the matrix material [16]. Hydrogen has significant solubility in molten aluminum, and high concentration of hydrogen causes porosity defects in the cast specimen.

Hexachloroethane (C_2Cl_6) tablets are used to remove hydrogen from the melt. Dried tablets are held with tongs and immersed in the melt inside the crucible. The tongs are held just above the crucible bottom and 5 min (approx.) is given for the decomposition of the tablet that ensures efficient hydrogen removal throughout the melt. The tablet decomposes and forms aluminum chloride ($AlCl_3$) bubbles in the melt that entraps the hydrogen gas and rises to the melt surface to expel the hydrogen gas to the atmosphere [17]. Granular cleaning flux is then added into the melt to remove the other non-metallic inclusions and oxides from the melt. The melt surface is then skimmed by using a skimmer. The reinforcement particles (B_4C and MoS_2) are mixed in an aluminum agate mortar and pestle, and the particles mixture is preheated and maintained at 300 °C. A detachable stainless steel stirrer is fixed over the furnace and immersed into the melt. The stirrer is run at the speed of 450 rpm to form a vortex [18]. The predetermined amount of reinforcement particles is added into the vortex of the melt. The stirring holds the reinforcement particles in suspension throughout the melt that helps to attain a homogenous distribution of the reinforcement particles in the matrix material. After the addition of particles, stirring is further continued for 1500 sec. The composite melt is then poured into the mold by

Fig. 1. Macrographs of (a) Stir casting equipment (1. Argon gas cylinder, 2. Electric furnace, 3. Stirrer, 4. Control unit and 5. Mild steel mold), (b) Flow of the composite melt (1. Melt and 2. Mild steel mold) and (c) Dismantled mild steel mold (1. Cast specimen).

bottom pouring through the pouring valve that is opened by actuating the lever. Fig. 1(b) shows the flow of composite melt. The hybrid composite is solidified at atmospheric conditions. Fig. 1(c) shows the stir cast hybrid composite within the dismantled mold. In an earlier work, the authors reported in detail the stir casting procedure of the mono composite [6].

3. Testing and characterization scheme

The details of hardness tests, fracture toughness tests, and tribotests conducted in the present work are explained in the following sections.

3.1. Hardness tests

The hybrid composite specimens for the hardness tests were polished using 400, 600 and 1000 grit abrasive sheets. The hardness of the mono and hybrid composite specimens was measured using a Brinell hardness tester. The carbide ball indenter was pressed at a test force of 500 kg for a dwell time of 15 sec at five different locations on the specimen surfaces. The mean of five hardness readings was used to plot the graph. Standard deviation is indicated by the error bars.

3.2. Fracture toughness tests

The Compact Tension (CT) specimens were machined from the bulk composites as per the dimensions are shown in Fig. 2. The fracture toughness tests were conducted using a Universal Testing Machine (UTM).

The dimensions were based on the standard proportions and tolerances mentioned in the ASTM standard E399-12e3 for CT specimens [19]. Starter notch was machined in the specimens to ensure the initiation of crack at the right place [20]. The tensile load is applied to test the specimens, and each composite specimen was tested three times, and the mean of the three test results was used to plot the graph. The error bars show the standard deviation.

3.3. Tribotests

The dry sliding wear tests were performed using a pin-on-disk type tribotester (Ducom, TR-20 LE). Tests were done in adherence to ASTM G99-05(2010) standard under atmospheric conditions (1 atm., and 30 ± 1 °C) for the sliding speeds of 0.5, 1, 1.5, 2 and 2.5 m/s, the applied load of 20 N and sliding distance of 1000 m. The test specimen was a cylindrical pin of 8 mm diameter and 30 mm in height. The pin surfaces were rough polished using 600 grit SiC abrasive sheets to reduce the protrusion of B_4C particles that may cause the microcutting of the counterface at the beginning of sliding [21]. EN 31 bearing steel disc (C – 0.99, Mn – 0.35, Si – 0.25, P – 0.025, S – 0.025, Cr – 1.40, Mo – 0.1, Ni – 0.25, Cu – 0.35, and the rest Fe by wt. %), supplied by M/s. Ducom Instruments, India, was used as the counterface whose hardness and surface roughness were 65 HRC and 0.1 µm, respectively. The weight loss after each test was quantified at a sensitivity of 0.1 mg using a precision balance (Sartorius, Secura 613-1S). The wear rate is computed using the formula $W = \delta W/S$ where W is the wear rate in mg/m,

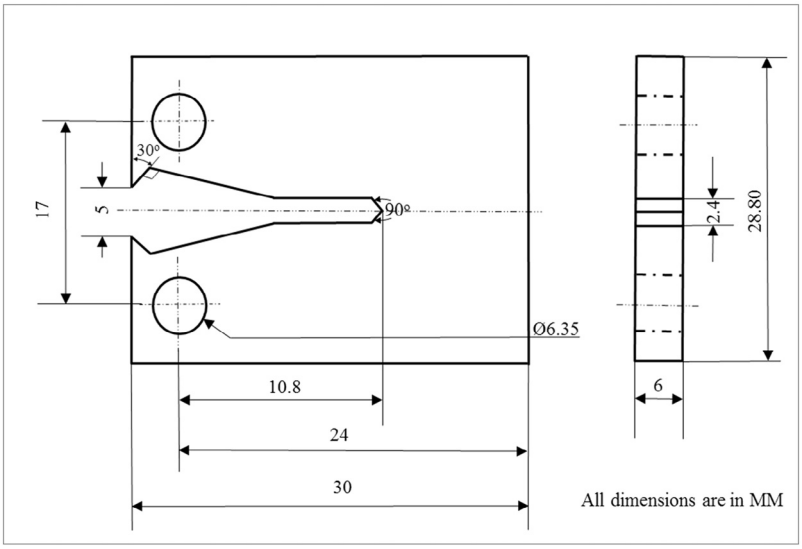

Fig. 2. Schematic of the CT specimen used for fracture toughness tests.

δW is the weight difference of the pin specimen before and after the test in mg and S is the sliding distance in m. Each test was repeated three times to confirm the repeatability of the tests, and the mean of three readings was used to plot the graphs and error bars show the standard deviation.

In this work, the tribological properties of the AA6061-10 wt. % B_4C mono composite [6] and AA6061-10 wt. % B_4C–MoS_2 hybrid composites reinforced with 2.5, 5 and 7.5 wt. % MoS_2 particles were compared to understand the influence of MoS_2 particles addition.

3.4. Characterization scheme

The distribution of reinforcement particles (B_4C and MoS_2) in the matrix material was analyzed using an Optical Microscope (Olympus, BX-51) and an X-ray powder diffractometer (Panalytical, Empyrean). The worn pin surfaces were characterized using a Scanning Electron Microscope (SEM, Hitachi, SU6600). The 3D surface profiles (evaluation area – 106 × 106 μm) of the worn pin surfaces and the mean surface roughness (S_a) were obtained using a laser microscope (Olympus, 3D measuring laser microscope LEXT OLS4000).

4. Results and discussion

In the following sections, the metallographic analysis, hardness, fracture toughness, and tribological properties of the hybrid composites are discussed.

4.1. Metallographic analysis

Metallographic specimens are cut from the bulk hybrid composites using a precision micro cutting machine which is equipped with a diamond wafer blade. The polishing process is carried out manually by using the metallographic grinding and polishing machine. The specimens are ground using SiC abrasive coated grinding discs of grit sizes 240, 320, 400, 500, 600, 800 and 1000. Water is sprayed continuously over the disc to act as a lubricant during grinding. After each grinding step, the specimen is swabbed with cotton soaked in warm water which is kept at 80 °C. After the final grinding step, in addition to the process of swabbing the specimen surface with soaked cotton, the specimen surface is sprayed with ethanol and dried. The specimens are polished with the diamond paste of grades 6, 3, and 1-microns, respectively to remove the damages caused by grinding. The diamond paste is manually applied and spread over the synthetic velvet cloth with the long nap. A new polishing cloth is used for each diamond paste grade to avoid scratches on the specimen surface. Diamond extender is used as the lubricant, and the paste is replenished for every few minutes. The lubricant prevents the heat generation during polishing and maintains the polishing cloth in the moist condition. Also, it enables the diamond abrasive particles to roll and slide freely between the specimen surface and the cloth.

The specimens are etched with Dix-Keller's reagent (2 ml hydrofluoric acid, 3 ml hydrochloric acid, 5 ml nitric acid and 190 ml distilled water) to enhance the microstructural features. Etching is done by swabbing.

The specimens are held in plastic tongs, and its surface is swabbed using the reagent saturated cotton (surgical grade) that is held in another plastic tongs. Etching is stopped as the suitable degree of dulling is exhibited by the specimen surface. Then the specimens are cleaned first with water and then with ethanol, and dried. Fig. 3 shows the specimens prepared for the metallographic analysis. Fig. 4(a)–(c) shows the metallographs of the 2.5, 5 and 7.5 wt. % MoS_2 hybrid composites. Distribution of reinforcement particles in the AA6061 matrix material is observed from the metallographs. Details of the metallographic analysis of AA6061-10 wt. % B_4C mono composite are available in an earlier work [6].

4.2. X-ray diffraction analysis

Fig. 5 shows the X-ray diffraction patterns of the 2.5, 5 and 7.5 wt. % MoS_2 hybrid composites. The diffraction patterns

Fig. 3. Macrograph showing the metallographic specimens of the hybrid composites (1. AA6061-10 wt. % B_4C–2.5 wt. % MoS_2, 2. AA6061-10 wt. % B_4C–5 wt. % MoS_2 and 3. AA6061-10 wt. % B_4C–7.5 wt. % MoS_2).

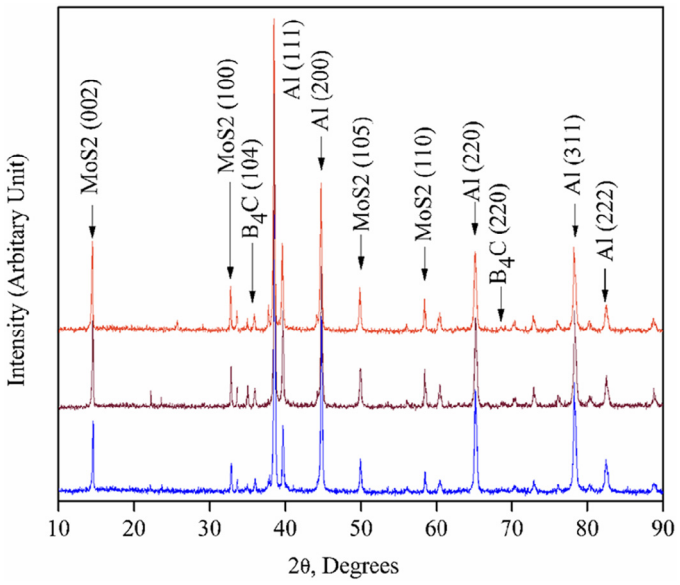

Fig. 5. X-ray diffraction patterns of AA6061-10 wt. % B_4C–MoS_2 hybrid composites reinforced with 2.5, 5 and 7.5 wt. % MoS_2 particles.

reveal the presence of matrix material and reinforcement particles (B_4C and MoS_2).

Also, it is noted that there is no formation of intermetallic compounds due to the reaction between the matrix material and reinforcement particles. The X-ray diffraction pattern of the mono composite is also available in an earlier work [6].

4.3. Hardness studies

Fig. 6 shows the effect of MoS_2 addition on the hardness of the hybrid composites. It is evident that the hardness of the mono composite is higher than that of the hybrid composites. The hardness of the hybrid composites decreases gradually with increase in MoS_2 particles addition.

The decrease in hardness with the increase in MoS_2 particles addition is attributed to the lubrication property of the MoS_2 particles which facilitates ease movement of grains along the slip planes due to which the specimen deforms easily under the indenter of the hardness tester [22].

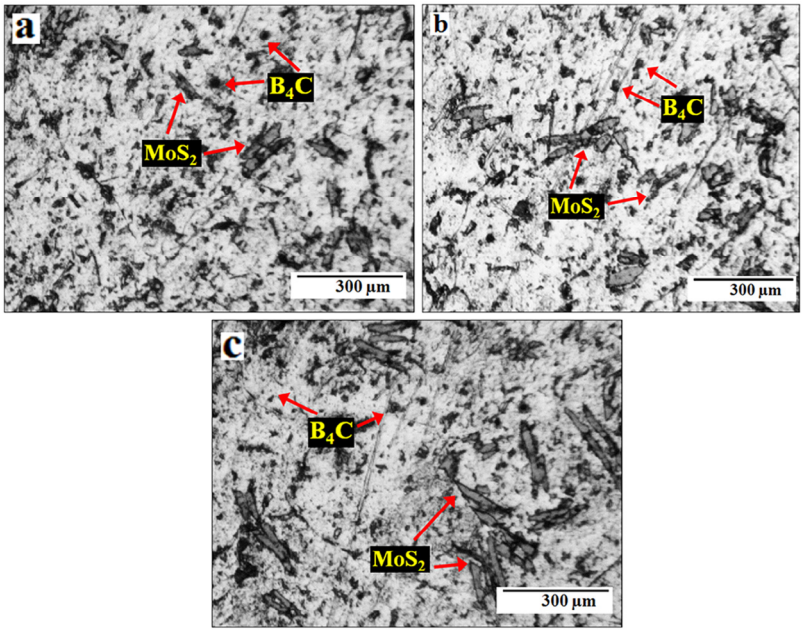

Fig. 4. Metallographs of the hybrid composites: (a) AA6061-10 wt. % B_4C–2.5 wt. % MoS_2, (b) AA6061-10 wt. % B_4C–5 wt. % MoS_2 and (c) AA6061-10 wt. % B_4C–7.5 wt. % MoS_2.

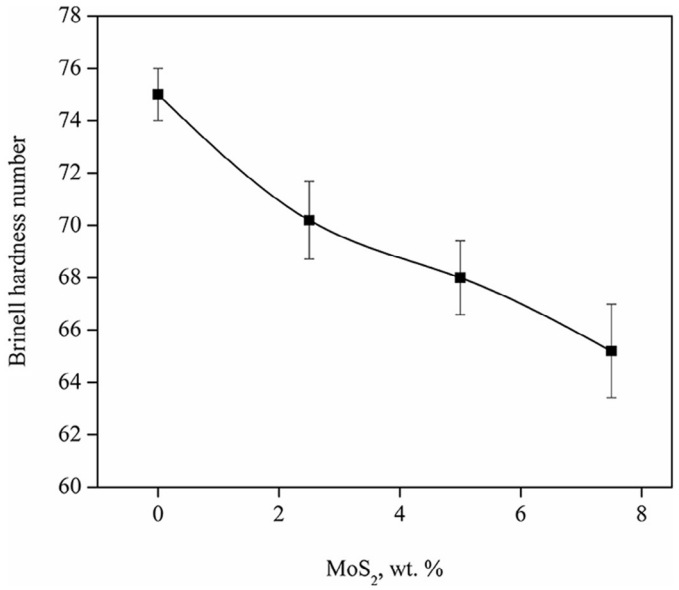

Fig. 6. Hardness of the AA6061-10 wt. % B_4C mono composite and AA6061-10 wt. % B_4C–MoS_2 hybrid composites reinforced with 2.5, 5 and 7.5 wt. % MoS_2 particles.

4.4. Fracture toughness studies

Fig. 7 shows the effect of MoS_2 addition on the fracture toughness of the hybrid composites. The fracture toughness decreases with increase in MoS_2 particles addition.

The fractograph of the 7.5 wt. % MoS_2 hybrid composite which is shown in Fig. 8 reveals the particles segregation (marked with arrow). In a particles segregated region, the inter-particle spacing is low, and the matrix material is very less. Ease of propagation of the crack through the particles segregated region enhances the fracture process which leads to the reduction in fracture toughness of the composites and the failure is predominantly due to intergranular brittle fracture as observed in Fig. 8.

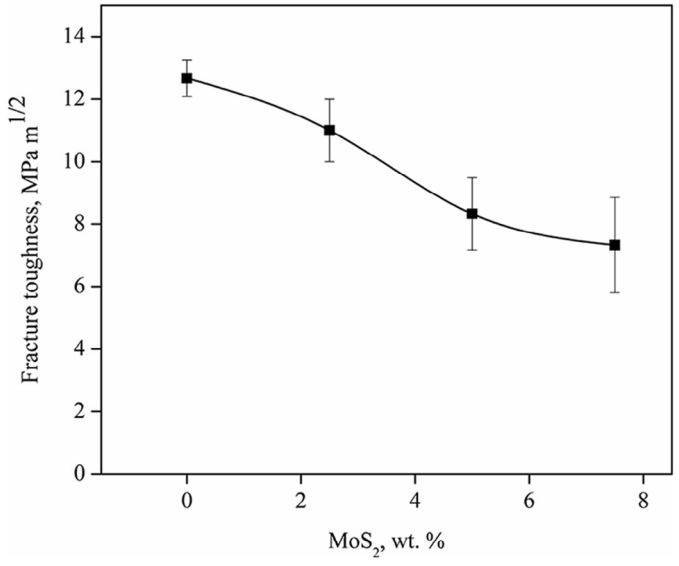

Fig. 7. Variation of fracture toughness of the AA6061-10 wt. % B_4C mono composite and AA6061-10 wt. % B_4C–MoS_2 hybrid composites reinforced with 2.5, 5 and 7.5 wt. % MoS_2 particles.

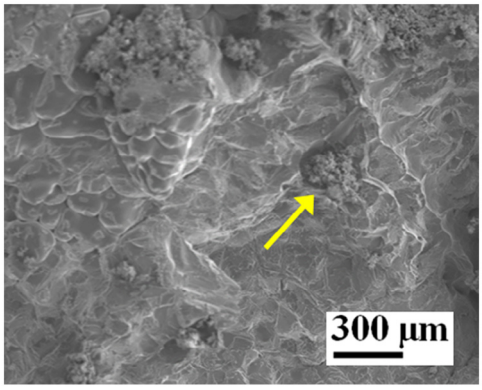

Fig. 8. SEM fractograph of AA6061-10 wt. % B_4C–7.5 wt. % MoS_2 hybrid composite showing segregation of reinforcement particles (marked with arrow).

4.5. Tribological studies

In this section, the influence of sliding speed and concentration of MoS_2 particles on the wear rate and friction coefficient are discussed.

4.5.1. Effect of sliding speed on wear rate

Fig. 9 shows the variation of wear rate with sliding speed for a fixed sliding distance of 1000 m and applied load of 20 N. It is inferred from Fig. 9 that for all the hybrid composites studied, the wear rate decreases with sliding speed, up to 2 m/s which is attributed to the formation of MoS_2-lubricated tribolayer between the contact surfaces. Also, Subramanian [23] observed that the increase in sliding speed causes the increase in strain rate which, in turn, increases the hardness. The increase in

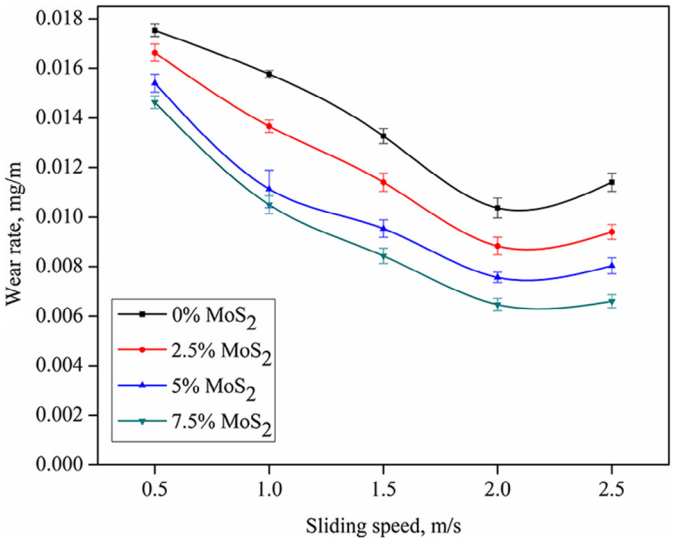

Fig. 9. Variation in wear rate as a function of sliding speed (sliding distance of 1000 m and applied load of 20 N).

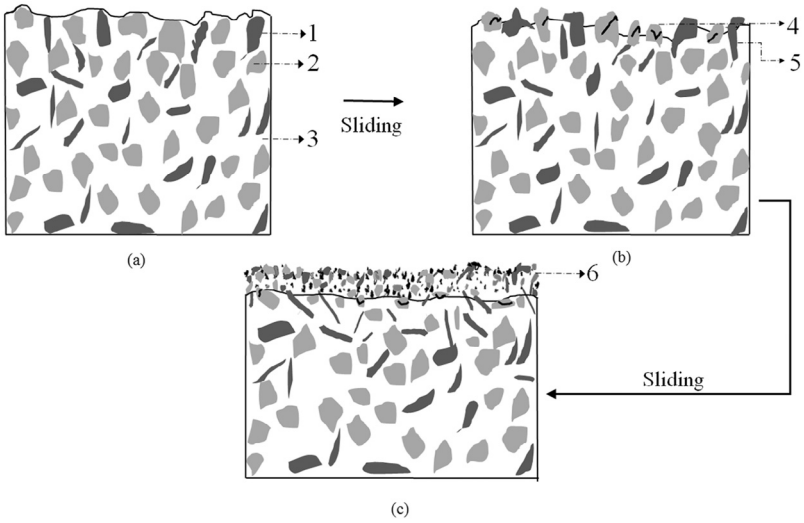

Fig. 10. Schematic showing (a) Pin surface of 7.5 % hybrid composite, (b) Squeezing of MoS_2 particles and microcracking of B_4C particles and (c) Formation of MoS_2-lubricated tribolayer (1. MoS_2 particle, 2. B_4C particle, 3. Matrix material, 4. Cracked B_4C particle, 5. Squeezed MoS_2 particle and 6. MoS_2-lubricated tribolayer).

hardness reduces the true area of contact between the tribo-couple contact surfaces which leads to decrease in wear rate.

Fig. 10(a) shows the schematic of the 7.5 wt. % MoS_2 hybrid composite pin surface before sliding. During sliding, the sub-surface plastic deformation causes the MoS_2 particles to squeeze onto the worn pin surface [24] (refer to Fig. 10b) and micro-cracks are formed on the B_4C particles (refer to Fig. 10b) which lead to its fracture into fine particles. Similar observation of cracking of ceramic particles into fine sized particles was reported by Sannino and Rack [25] for Al–SiC_p and 17-4 PH tribo-couple during sliding. The squeezed MoS_2 particles get smeared and mixed with debris on the contact surfaces and get transferred back and forth with the debris between the tribo-couple which, in turn, leads to the formation of MoS_2-lubricated tribolayer as shown in Fig. 10(c). MoS_2-lubricated tribolayer formed on the worn pin surface of the 7.5 wt. % MoS_2 hybrid composite is shown in Fig. 11(a). Fig. 11(b) shows the BSE micrograph which depicts the smeared MoS_2 particles (marked with arrow) and Fig. 11(c) shows the high magnification BSE micrograph which illustrates the interface between the smeared MoS_2 particles and the matrix material debris (marked with dotted line). In the case of a mono composite, the

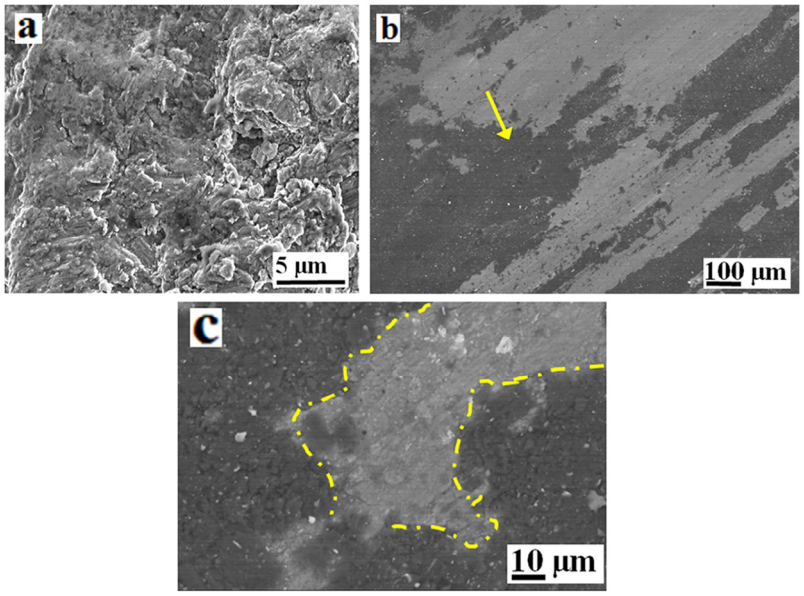

Fig. 11. SEM micrograph of 7.5 wt. % MoS_2 hybrid composite worn pin surface: (a) MoS_2-lubricated tribolayer, (b) BSE micrograph showing smeared MoS_2 particles (marked with arrow) and (c) High magnification BSE micrograph showing interface between smeared MoS_2 particles and matrix material debris (marked with dotted line) (sliding speed 0.5 m/s, applied load 20 N and sliding distance 1000 m).

microcracked fine B_4C particles get mixed with the debris to form Mechanically Mixed Layer (MML) to provide solid lubrication [6].

As the sliding speed increases beyond 2 m/s, the wear rate is increased due to the friction-induced temperature rise which softens the hybrid composite materials to undergo severe plastic deformation [23]. This phenomenon, in turn, causes the incurrence of shear fracture in the subsurface which disintegrates the MoS_2-lubricated tribolayer. Consequently, metallic contact is established between the tribo-couple contact surfaces leading to the increase in wear rate due to the induction of delamination wear mechanism.

Fig. 12(a) shows the delaminated worn pin surface of 5 wt. % MoS_2 hybrid composite. The material is removed in the form of platelet-shaped particles from the worn pin surface which consequently leads to the formation of a shallow crater. A dotted curve is drawn on the worn pin surface to separate the un-delaminated surface region and the delaminated surface region having the shallow crater. Also, sliding grooves (marked with arrow) are observed throughout the shallow crater surface, and Fig. 12(b) shows the high magnification micrograph which illustrates the region marked with the dotted ellipse on Fig. 12(a). It shows the crack propagation (marked with arrow) through the worn pin surface. The propagation of the crack leads to the production of delaminated debris due to the delamination mechanism. Fig. 12(c) shows a delaminated particle (marked with arrow) which is attached scantly to the worn pin surface. The presence of shallow sliding grooves (marked with dotted arrow) is also evident. Fig. 12(d) shows the high magnification micrograph of Fig. 12(c), which illustrates the presence of a crack (marked with arrow) and cross-hatching (marked with dotted arrow) on the surface of the delaminated

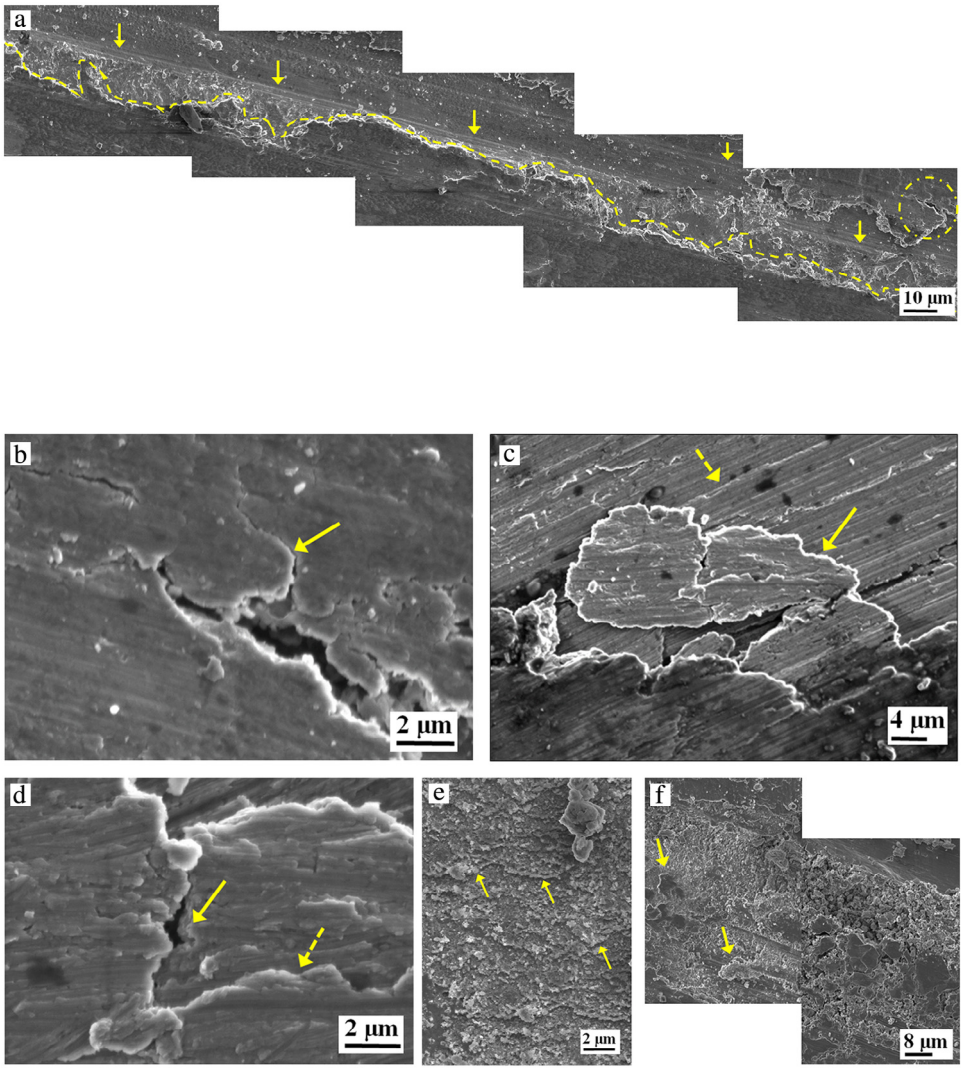

Fig. 12. SEM micrographs showing (a) Long shallow crater surface (dotted curve divides the delaminated and un-delaminated surface regions), sliding grooves (marked with arrow) and region of crack propagation (marked with dotted ellipse). (b) High magnification micrograph showing propagation of crack (marked with arrow). (c) Delaminated particle (marked with arrow) and sliding grooves (marked with dotted arrow). (d) High magnification micrograph showing crack (marked with arrow) and cross-hatching (marked with dotted arrow). (e) Cross-hatchings on shallow crater surface (marked with arrow). (f) Severely damaged region and cross-hatchings (marked with arrow) on the worn pin surface of 5 wt. % MoS_2 hybrid composite (sliding speed 2.5 m/s, applied load 20 N and sliding distance 1000 m).

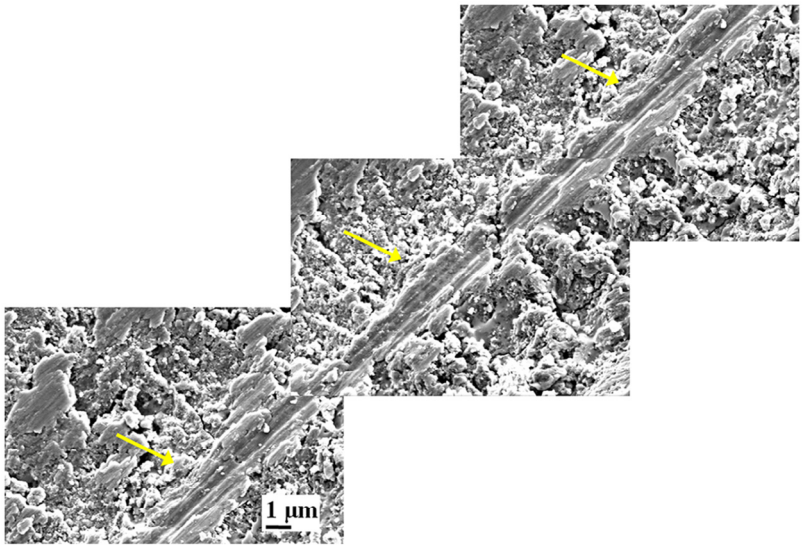

Fig. 13. SEM micrograph showing a continuous and narrow relatively undamaged strip (marked with arrow) on the severely damaged worn pin surface of 7.5 wt. % MoS_2 hybrid composite (sliding speed 2.5 m/s, applied load 20 N and sliding distance 1000 m).

particle. Fig. 12(e) shows the high magnification micrograph of Fig. 12(a), which depicts the cross-hatchings (marked with arrow) on the shallow crater surface.

As the sliding speed is increased from 2 to 2.5 m/s, abrasion is also observed on the worn pin surface. Fig. 12(f) shows the abrasion induced severe damage and cross-hatchings (marked with arrow) on the worn pin surface. The platelet-shaped delaminated debris is formed by the growth of the cross-hatchings.

Fig. 13 shows the abrasion induced severely damaged worn pin surface of 7.5 wt. % MoS_2 hybrid composite having relatively undamaged continuous and narrow strip (marked with arrow) which may be formed due to the lubrication offered during sliding by the MoS_2 particles entrapped between the tribo-couple. The increase in sliding speed from 2 to 2.5 m/s leads to the abrading of the counterface by B_4C particles which lead to the formation of counterface debris (marked with arrow) as shown in Fig. 14(a). The wear debris of the pin specimen is also seen in the form of debris lumps (marked with dotted arrow).

The edges of the counterface debris are cleaved throughout its circumference as shown in the high magnification micrograph of Fig. 14(b). EDS spectrum revealed the chemical composition (Fe 49.95, Al 22.04, O 27.56 and Cr 0.46) of the counterface debris where the dominant constituent is Fe. Chip-like debris is also produced with the increase in sliding speed. Fig. 15(a) shows chip-like debris of 5 wt. % MoS_2 hybrid composite. The region marked with dotted circle in Fig. 15(a) is shown in the high magnification micrograph of Fig. 15(b) which depicts layers of overlapping matrix material (marked with arrow). Cavities (marked with dotted arrow) and cracks (marked with open arrow) are also observed. A high magnification micrograph of Fig. 15(b) shown in Fig. 15(c) depicts shallow sliding grooves (marked with arrow) on the debris surface. Fig. 16 shows flow-type chip debris having lamella structure which is formed due to the abrasion [26].

Fig. 17 shows the worn pin surface of 7.5 wt. % MoS_2 hybrid composite which illustrates the presence of wear debris clusters (marked with arrow) scattered on the worn pin surface. The wear debris clusters constitute the remaining of the disintegrated MoS_2-lubricated tribolayer. It is observed from Fig. 17 that the worn pin surface is relatively undamaged on the regions where the wear debris clusters are scattered. Also, cracks (marked with dotted arrow) are observed on the worn pin surface regions where the wear debris clusters are not present.

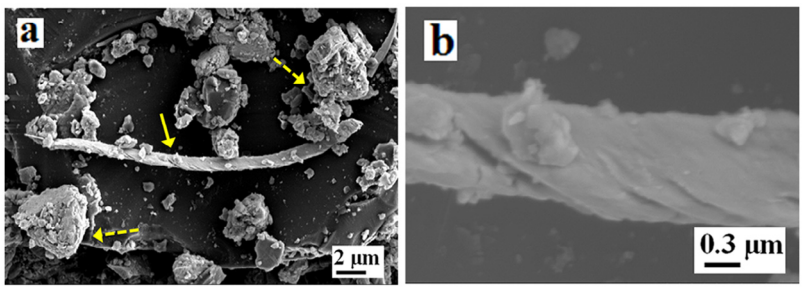

Fig. 14. SEM micrograph showing (a) Counterface debris (marked with arrow) and wear debris (marked with dotted arrow) of 7.5 wt. % MoS_2 hybrid composite and (b) High magnification micrograph showing cleaved circumferential edges of the counterface debris (sliding speed 2.5 m/s, applied load 20 N and sliding distance 1000 m).

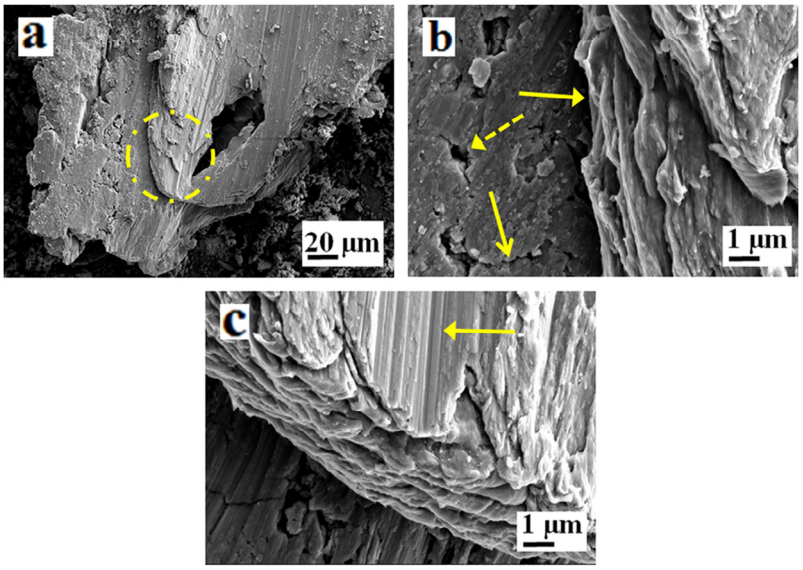

Fig. 15. SEM micrograph showing (a) Chip-like debris and region of overlapping matrix material (marked with dotted ellipse), (b) High magnification micrograph showing cavities (marked with dotted arrow), cracks (marked with open arrow) and overlapping matrix material (marked with arrow) and (c) High magnification micrograph showing sliding grooves (marked with arrow) of 5 wt. % MoS_2 hybrid composite (sliding speed 2.5 m/s, applied load 20 N and sliding distance 1000 m).

During sliding, some of the wear debris released from the tribo-couple contact area move towards the periphery of the counterface. However, some wear debris will adhere to the worn pin surface as shown in Fig. 18(a). It is observed that the wear debris made a trail (marked with arrow) as it moved from one place on the worn pin surface to the other. Fig. 18(b) shows the distance between the possible originating region and the present position of the debris as 114 µm (marked with up down arrow with base on both ends).

Fig. 19(a) and (b) shows the worn pin surface of the mono composite and its corresponding 3D surface profile. Fig. 20(a) and (b) shows the worn pin surface of the 7.5 wt. % MoS_2 hybrid composite and its corresponding 3D surface profile. The 3D surface profile of the mono composite is rougher due to the distinct sliding grooves (refer to Fig. 19(a)) observed on the worn pin surface. In comparison, the 3D surface profile of the 7.5 wt. % MoS_2 hybrid composite is smoother due to the shallow sliding grooves (refer to Fig. 20(a)) observed on the worn pin surface. Also, at the sliding speed of 2.5 m/s, the mean surface roughness (S_a) of the mono composite is 3.532 µm which is higher than that of the 7.5 wt. % MoS_2 hybrid composite. S_a value of the 7.5 wt. % MoS_2 hybrid composite is 1.317 µm. Smoothening of the contact surfaces by the smeared

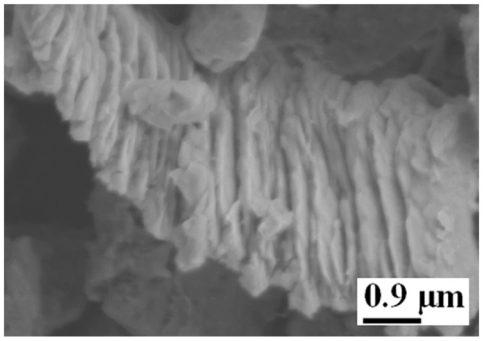

Fig. 16. SEM micrograph showing flow-type chip debris having lamella structure of 5 wt. % MoS_2 hybrid composite (sliding speed 2.5 m/s, applied load 20 N and sliding distance 1000 m).

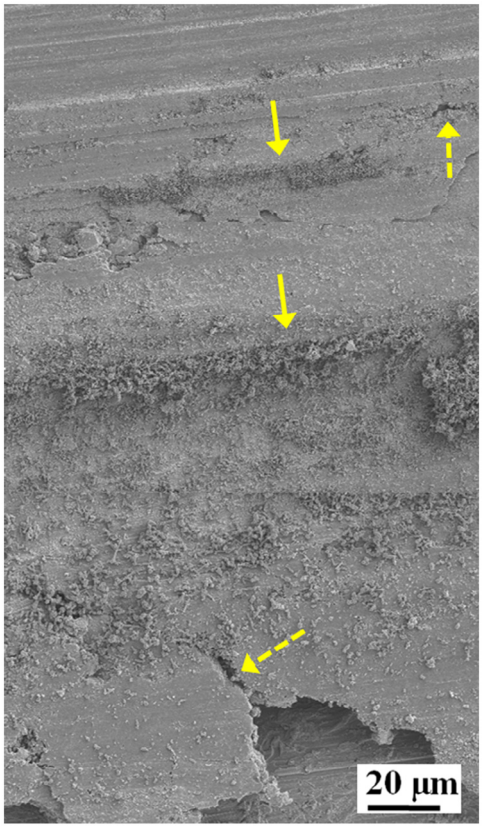

Fig. 17. SEM micrograph showing wear debris clusters (marked with arrow) and cracks (marked with dotted arrow) on the worn pin surface of 7.5 wt. % MoS_2 hybrid composite (sliding speed 2.5 m/s, applied load 20 N and sliding distance 1000 m).

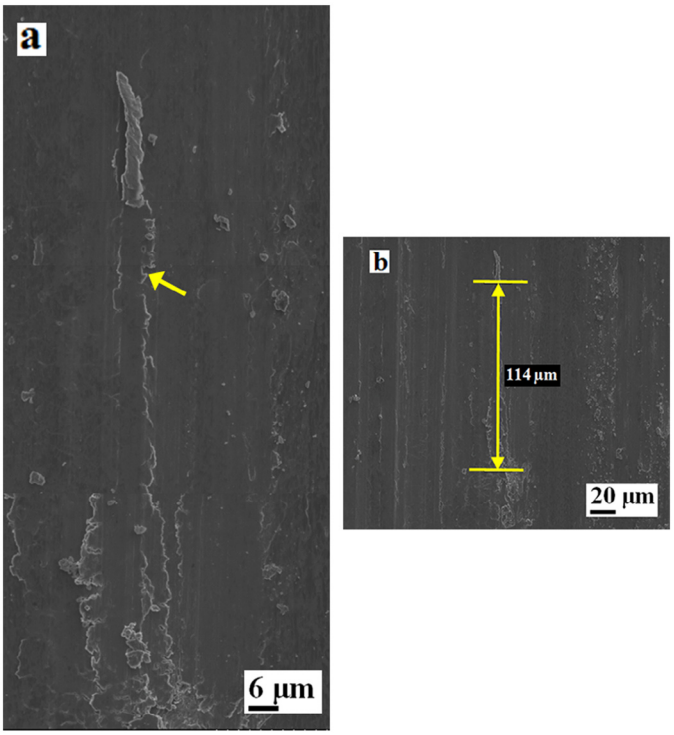

Fig. 18. SEM micrographs showing (a) Trail of the wear debris (marked with arrow) and (b) Distance traveled by the wear debris (marked with up down arrow with base on both ends) of 5 wt. % MoS_2 hybrid composite (sliding speed 2.5 m/s, applied load 20 N, sliding distance 1000 m).

MoS_2 particles reduces the S_a value of the hybrid composite compared to that of the mono composite.

4.5.2. *Effect of sliding speed on friction coefficient*

Fig. 21 shows the variation of friction coefficient with sliding speed for a fixed sliding distance of 1000 m and applied load of 20 N. It is inferred from Fig. 21 that all the hybrid composites exhibited the decrease in the friction coefficient with the increase in sliding speed up to about 2 m/s due to the solid lubrication provided by the MoS_2-lubricated tribolayer. As the sliding speed increases from 2 to 2.5 m/s, the friction coefficient is increased. The wear rate is also increased for the same sliding speed range of 2–2.5 m/s due to delamination. The platelet-shaped delaminated wear debris causes severe destruction on the worn pin surface which leads to the increase in friction coefficient. Ma and Lu [27] studied the tribological properties of Cu–Gr composites and observed that for the sliding speed range of 0.5–8 m/s, the specific wear rate and friction coefficient are increased. This finding is nearly similar to the observation made in the present work for the sliding speed range of 2–2.5 m/s.

Formation of MML reduced the friction coefficient for the mono composite up to 2 m/s [6] beyond which it is increased due to the friction induced by the sliding of delaminated debris in between the tribo-couple contact surfaces. The mono composite exhibits higher friction coefficient compared to that of

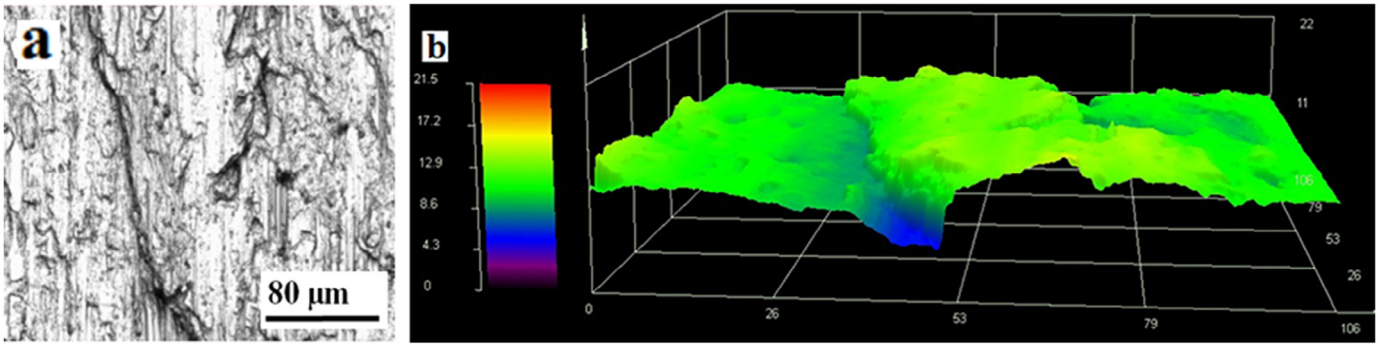

Fig. 19. Confocal laser microscopy images showing (a) Worn pin surface and (b) 3D surface profile of mono composite (sliding speed 2.5 m/s, applied load 20 N and sliding distance 1000 m).

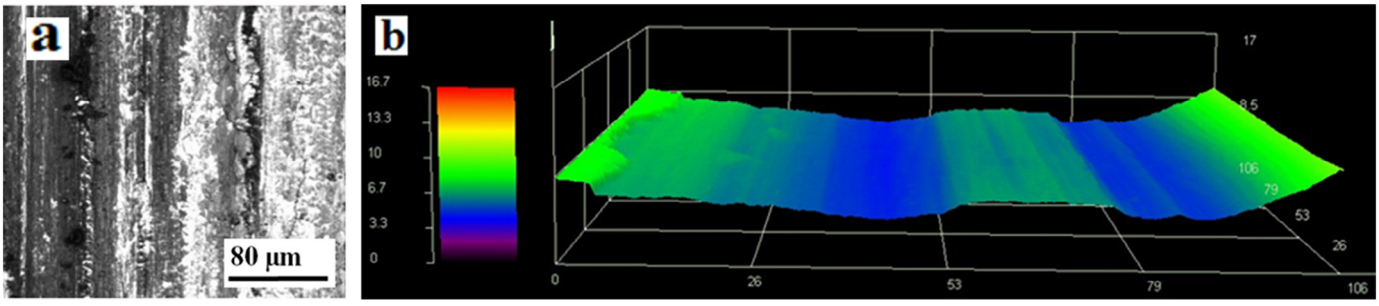

Fig. 20. Confocal laser microscopy images showing (a) Worn pin surface and (b) 3D surface profile of 7.5 wt. % MoS_2 hybrid composite (sliding speed 2.5 m/s, applied load 20 N and sliding distance 1000 m).

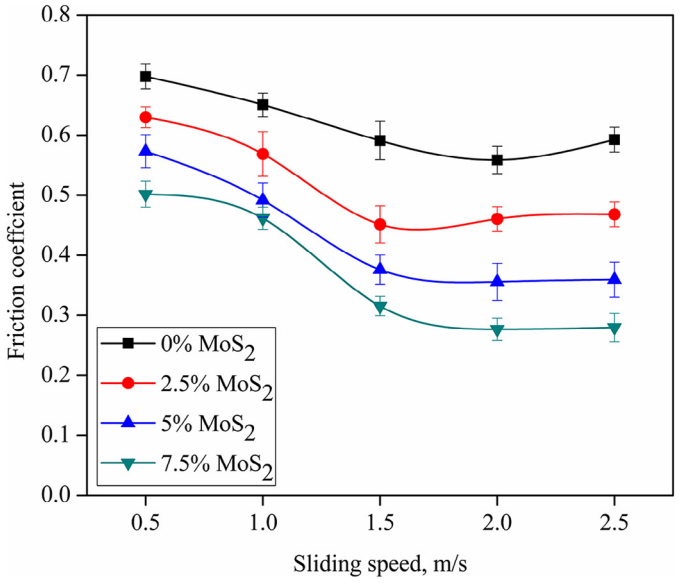

Fig. 21. Variation in friction coefficient as a function of sliding speed (sliding distance of 1000 m and applied load of 20 N).

the hybrid composites due to the absence of solid lubricant layer.

5. Conclusions

In summarizing the study on mechanical and tribological properties of AA6061-B_4C–MoS_2 hybrid composites the following inferences are derived.

- The hardness of the hybrid composites decreases monotonously with the increase in MoS_2 particles addition. The hybrid composites become easily deformable with the increase in MoS_2 particles concentration leading to a decrease in hardness.
- The fracture toughness of the hybrid composites is decreased with increase in MoS_2 particles addition. Fractograph of 7.5 wt. % MoS_2 hybrid composite reveals segregation of reinforcement particles which enhances the fracture process.
- Formation of MoS_2-lubricated tribolayer reduces the wear rate of the hybrid composites up to a sliding speed of 2 m/s, beyond which the wear rate is increased due to the disintegration of the MoS_2-lubricated tribolayer which leads to the induction of delamination and abrasion wear mechanisms.
- The presence of MoS_2 particles between the contact surfaces reduced the wear rate and friction coefficient of the hybrid composites compared to the mono composite. It is evident from the above study that the hybrid composites exhibited self-lubricating characteristics which make them resource-efficient materials.

Acknowledgements

The authors thank Dr. T.P.D. Rajan, CSIR–NIIST for his helpful suggestions on composites fabrication.

References

[1] G.S. Cole, A.M. Sherman, Light weight materials for automotive applications, Mater. Charact. 35 (1995) 3–9.
[2] S. Basavarajappa, G. Chandramohan, A. Mahadevan, M. Thangavelu, R. Subramanian, P. Gopalakrishnan, Influence of sliding speed on the dry sliding wear behavior and the subsurface deformation on hybrid metal matrix composite, Wear 262 (2007) 1007–1012.
[3] P. Ravindran, K. Manisekar, P. Rathika, P. Narayanasamy, Tribological properties of powder metallurgy – processed aluminium self lubricating hybrid composites with SiC additions, Mater. Design 45 (2013) 561–570.
[4] A.R. Kennedy, The microstructure and mechanical properties of Al-Si-B_4C metal matrix composites, J. Mater. Sci. 37 (2002) 317–323.
[5] A. Canakci, F. Arslan, Abrasive wear behavior of B_4C particle reinforced Al2024 MMCs, Int. J. Adv. Manuf. Technol. 63 (2012) 785–795.
[6] V.V. Monikandan, M.A. Joseph, P.K. Rajendrakumar, M. Sreejith, Tribological behavior of liquid metallurgy-processed AA 6061-B_4C composites, Mater. Res. Express 2 (2015) 1–11.
[7] S.V. Prasad, R. Asthana, Aluminum metal-matrix composites for automotive applications: tribological considerations, Tribol. Lett. 17 (2004) 445–453.
[8] V. Rajput, R.K. Gautam, R. Tyagi, Tribological behavior of Al based self-lubricating composites, in: M. J. B. Ghazali, M. F. B. Abdollah (Eds.), Proceedings of Malaysian International Tribology Conference, Malaysian Tribology Society, Kuala Lumpur, 2015, pp. 108–110.
[9] J. Deng, T. Can, J. Sun, Microstructure and mechanical properties of hot-pressed Al_2O_3/TiC ceramic composites with the additions of solid lubricants, Ceram. Int. 31 (2005) 249–256.
[10] H. Kato, M. Takama, Y. Iwai, K. Washida, Y. Sasaki, Wear and mechanical properties of sintered copper–tin composites containing graphite or molybdenum disulfide, Wear 255 (2003) 573–578.
[11] S. Dharmalingam, R. Subramanian, K.S. Vinoth, B. Anandavel, Optimization of tribological properties in aluminum hybrid metal matrix composites using Gray-Taguchi method, J. Mater. Eng. Perform. 20 (2011) 1457–1466.
[12] S. Dharmalingam, R. Subramanian, M. Kök, Optimization of abrasive wear performance in aluminium hybrid metal matrix composites using Taguchi–grey relational analysis, Proc. Inst. Mech. Eng. Part J 227 (2013) 749–760.
[13] L. Zhang, J. Xiao, K. Zhou, Sliding wear behavior of silver–molybdenum disulfide composite, Tribol. Trans. 55 (2012) 473–480.
[14] A.M. Kovalchenko, O.I. Fushchich, S. Danyluk, The tribological properties and mechanism of wear of Cu-based sintered powder materials containing molybdenum disulfide and molybdenum diselenite under unlubricated sliding against copper, Wear 290–291 (2012) 106–123.
[15] S. Dhanasekaran, R. Gnanamoorthy, Abrasive wear behavior of sintered steels prepared with MoS_2 addition, Wear 262 (2007) 617–623.
[16] S. Gopalakrishnan, N. Murugan, Production and wear characterisation of AA 6061 matrix titanium carbide particulate reinforced composite by enhanced stir casting method, Composites Part B 43 (2012) 302–308.
[17] J.R. Davis, Molten aluminum processing and casting, in: ASM Specialty Handbook: Aluminum and Aluminum Alloys, ASM International, Ohio, 1993, pp. 199–201.
[18] A. Canakci, F. Arslan, I. Yasar, Pre-treatment process of B_4C particles to improve incorporation into molten AA2014 alloy, J. Mater. Sci. 42 (2007) 9536–9542.
[19] ASTM E399-12e3, Standard Test Method for Linear-Elastic Plane-Strain Fracture Toughness KIc of Metallic Materials, ASTM International, West Conshohocken, PA, 2012.
[20] D. Broek, Plain strain fracture toughness, in: Elementary Engineering Fracture Mechanics, Martinus Nijhoff Publishers, The Hague, 1982, p. 172.
[21] Z. Zhang, L. Zhang, Y.-W. Mai, The running-in wear of a steel/SiCp-Al composite system, Wear 194 (1996) 38–43.
[22] K.W.H. Seah, S.C. Sharma, B.M. Girish, Mechanical properties of cast ZA-27/graphite particulate composites, Mater. Design 16 (1995) 271–275.
[23] C. Subramanian, Effects of sliding speed on the unlubricated wear behavior of Al-12.3wt.%Si alloy, Wear 151 (1991) 97–110.

[24] Y.B. Liu, S.C. Lim, S. Ray, P.K. Rohatgi, Friction and wear of aluminium-graphite composites: the smearing process of graphite during sliding, Wear 159 (1992) 201–205.
[25] A.P. Sannino, H.J. Rack, Surface topography evolution during sliding wear of 2009 Al-SiCp/17-4 PH, Wear 181–183 (1995) 202–211.
[26] A.W. Momber, Y.C. Wong, Geometrical features of wear debris Part 1 erosion of ductile steel by solid particle impingement, J. Mater. Sci. 40 (2005) 3517–3522.
[27] W. Ma, J. Lu, Effect of sliding speed on surface modification and tribological behavior of copper-graphite composite, Tribol. Lett. 41 (2011) 363–370.